

Hall instability driven seeding of helical magneto-Rayleigh–Taylor instabilities in axially premagnetized thin-foil liner Z-pinch implosions

Cite as: Phys. Plasmas **29**, 122701 (2022); <https://doi.org/10.1063/5.0103651>

Submitted: 16 June 2022 • Accepted: 06 November 2022 • Published Online: 02 December 2022

 J. M. Woolstrum,  C. E. Seyler and  R. D. McBride



View Online



Export Citation



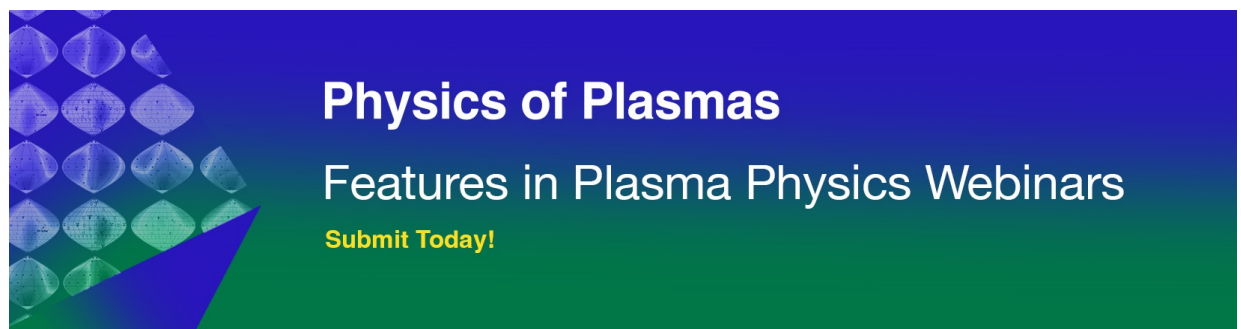
CrossMark

ARTICLES YOU MAY BE INTERESTED IN

[Announcement: The 2021 James Clerk Maxwell prize for plasma physics](#)
Physics of Plasmas **29**, 070201 (2022); <https://doi.org/10.1063/5.0106539>

[Wave-supported hybrid fast-thermal p-¹¹B fusion](#)
Physics of Plasmas **29**, 110701 (2022); <https://doi.org/10.1063/5.0119434>

[Modeling ablator grain structure impacts in ICF implosions](#)
Physics of Plasmas **29**, 112708 (2022); <https://doi.org/10.1063/5.0107534>



Hall instability driven seeding of helical magneto-Rayleigh–Taylor instabilities in axially premagnetized thin-foil liner Z-pinch implosions

Cite as: Phys. Plasmas **29**, 122701 (2022); doi: 10.1063/5.0103651

Submitted: 16 June 2022 · Accepted: 6 November 2022 ·

Published Online: 2 December 2022



View Online



Export Citation



CrossMark

J. M. Woolstrum,^{1,a)}  C. E. Seyler,²  and R. D. McBride¹ 

AFFILIATIONS

¹Nuclear Engineering and Radiological Sciences, University of Michigan, Ann Arbor, Michigan 48109, USA

²Laboratory of Plasma Studies, Cornell University, Ithaca, New York 14853, USA

^{a)}Author to whom correspondence should be addressed: jeffwool@umich.edu

ABSTRACT

Helical magneto-Rayleigh–Taylor instability (MRTI) structures have been observed in z-pinch-driven liner implosion experiments with a pre-imposed axial magnetic field. We show that the formation of these helical structures can be described by a Hall magnetohydrodynamical (HMHD) model. We used the 3D extended magnetohydrodynamics simulation code PERSEUS (which includes Hall physics) [Seyler and Martin, Phys. Plasmas **18**, 012703 (2011)] to study these helical instabilities and show that a Hall interchange instability in low-density coronal plasma immediately surrounding the dense liner is responsible for producing helically oriented effects in the magnetic field and current density within the coronal layer. This seeds the helical pitch angle of the MRTI even when other proposed helical seeding mechanisms are either not present in the experiments or not accounted for in the simulations. For example, this mechanism does not require low-density power-feed plasmas to be swept in from large radius or the development of electrothermal instabilities. The Hall Instability is, thus, a new, independent explanation for the origin of the helical instabilities observed in axially premagnetized liner experiments. Simulation results supporting this mechanism are presented.

Published under an exclusive license by AIP Publishing. <https://doi.org/10.1063/5.0103651>

I. INTRODUCTION

Z-pinchs have extensively been studied as a platform for Inertial Confinement Fusion (ICF), specifically as part of the Magnetized Liner Inertial Fusion (MagLIF)^{1,2} efforts on the 100-ns, 20-MA Z machine at Sandia National Laboratories.³ MagLIF makes use of cylindrical metal tubes (liners) that are imploded using the strong electrical currents produced by the Z machine. These currents are directed axially along the liner's outer surface. This creates a $\mathbf{J} \times \mathbf{B}$ force density that drives the implosion radially inward.^{4,5} These liners, which have an initial radius of about 3 mm, a wall thickness of about 0.5 mm, and a height of about 10 mm, are unstable to the acceleration-driven magneto-Rayleigh–Taylor (MRT) instability (MRTI)^{6–27} and to magnetic-compression-driven instabilities such as the $m = 0$ “sausage mode,” the $m = 1$ “kink mode,” and general $m \geq 1$ helical modes, where m is the azimuthal mode number that also represents the number of intertwined helices in the instability structure.^{8,13,14,16} These are fast-growing instabilities that are detrimental to implosion uniformity and, thus, to efforts in magnetically driven ICF.^{1,8,12,20,22,23,25}

In MagLIF, both the deuterium fuel and the liner are premagnetized with an axial magnetic field B_z (on the order of 10 T) to limit thermal conduction losses from the hot fuel to the cold liner. From penetrating radiography experiments on the Z machine, the combination of the premagnetizing B_z field with the implosion-driving B_θ field was found to result in helical instability structures with $m \approx 6$.⁸

To study metal liner implosion instabilities on a university-scale pulsed power machine (~ 1 MA in ~ 100 ns) requires significantly less mass in the liner. Because of this, liners are constructed by wrapping an ultrathin sheet of metal foil (e.g., 400-nm-thick aluminum) around a dumbbell-shaped support structure. The supported thin-foil liner is then installed between the anode and cathode of a pulsed power machine. Thin-foil liners of this type have been used in experiments on the MAIZE facility at the University of Michigan^{11,13,14,28} and on the COBRA facility at Cornell University.^{17,26} The use of thin-foil liners on MAIZE and COBRA has enabled the study of helical instability structures like those seen in MagLIF experiments on the Z facility.

We note that helical MRTI has also been observed in axially premagnetized gas-puff z-pinch implosions.¹⁰

The origin of helical instabilities in axially premagnetized liner implosions is a topic of ongoing research within the community and has several proposed explanations ranging from low-density power-feed plasma being swept in from large radius and compressing the pre-imposed axial magnetic field up against the liner's outer surface^{15,29} to electrothermal instability (ETI) effects.^{8,12,28,30}

In this paper, we present a new explanation for the origin of helical instabilities in thin-foil z-pinch. We propose a form of the Hall Instability of the interchange type that causes a series of effects including current advection, current filamentation, and magnetic field advection. These processes occur in a low-density coronal plasma layer that surrounds the dense liner plasma. The helical perturbations that form in the coronal plasma are found to seed the helical MRTI that eventually develops in the dense liner plasma as the liner implodes. Importantly, this explanation does not require low-density plasma to be present at large radius in the power feed of the pulsed power machine. This is important because experiments conducted at the university scale (~ 1 MA) have found very little plasma formation in power feeds (unless something very deliberate is done to generate the plasma, as was done in Ref. 31, where thick dielectric structures were covered with thin metal foils to source significant plasma), and yet helical instability structures still develop in axially premagnetized experiments at the 1-MA level.¹⁴ The background density in thin-foil liner and gas puff z-pinch experiments on MAIZE is vacuum and is $\sim 10^{-5}$ Torr or $\sim 3 \times 10^{11}$ cm⁻³. This is lower than the achievable density floor of the version of PERSEUS used in this study (3×10^{13} cm⁻³). The floor density plasma is not allowed to move to preserve its positivity. If the floor was able to be lowered enough to account for plasma on the order of $\sim 3 \times 10^{11}$ cm⁻³, then some small amount of flux compression might be expected. It should be noted that as the density floor is lowered to zero, kinetic effects within that regime will become increasingly important and even fully two-fluid codes will be inadequate to completely capture the effects of the plasma at that density scale. However, due to the limitations of the minimum density floor achievable by the version of PERSEUS used in this study, and due to the fact that PERSEUS is fundamentally a fluid code (and not kinetic), we are unable to capture these potential effects. Additionally, this new explanation does not require solid-metal ETI effects, as the solid-metal state of the thin-foil liner was not modeled in these simulations. Although this new explanation does not require low-density plasma at large radius in the power feed (as appropriate for 1-MA experiments), we note that at higher currents (e.g., the 30-MA Z machine), low-density power-feed plasmas could very well be present at large radius, and thus, they could still play an important role in the development of helical instabilities, as shown in Ref. 15. While the simulations in Ref. 15 did not have a coronal layer initialized, it is possible that the effects were present in those simulations as well. However, as the Hall instability effects were not known at the time of the Ref. 15 study, their relative contribution was not studied. Also, it is important to note that the proposed Hall seeding mechanism of the present work does not preclude the flux compression seeding mechanism of Ref. 15. In fact, the true seeding mechanism of MagLIF liners may be a combination of several different seeding effects. This may be true of the thin-foil liners as well, where the Hall effects in this paper may work in conjunction with other effects to seed the helical MRTI observed in experiment.

For thin-foil liner implosions at the 1-MA level, the coronal plasma layer hypothesis is further supported by the recent experimental work,^{32,33} where a coronal plasma layer has been found to form around current-carrying thin-foils due to surface contaminant blow-off and outgassing. We also note that these coronal plasma layers could potentially form around thick-walled MagLIF liners on the Z facility as well, due to the high current densities generated on the Z facility.

The Hall interchange instability and its effects were explored theoretically in Refs. 34 and 35. The dynamics of this instability in a z-pinch context, and how these effects may seed helical MRTI in thin-foil liner implosions, are the subjects of this paper.

The remainder of this paper is organized as follows. In Sec. II, we present the simulation setup. In Sec. III, we present a reduced Hall MHD model. From this model, a theoretical dispersion relation is derived for the Hall interchange instability. This relation is then used to generate instability growth rate results that are compared with those from simulations. In Sec. IV, we explore the dynamics of the coronal plasma layer, as simulated in PERSEUS,³⁶ and show that this coronal layer can provide a seed for helical MRTI in the denser liner plasma. Here, we also make the argument that a Hall Instability can explain the behavior of the simulated coronal plasma. We use Hall Instability theory to show that, given the simulation parameters, a Hall Instability is expected to form. In Sec. V, we discuss various boundary condition (BC) effects. In Sec. VI, we compare results from simulations with and without Hall physics turned on to show that these are indeed Hall-driven effects. In Sec. VII, we discuss some of the subtleties of our work. In Sec. VIII, we summarize our work and provide recommendations for the future.

II. SIMULATION SETUP AND PARAMETERS

For the simulations presented herein, we used the 3D Eulerian extended magneto-hydrodynamics (XMHD) code PERSEUS, which was developed at Cornell University.³⁶ The version of the code used in this paper uses a fifth order finite volume method with a positivity preserving limiter that keeps the density and pressure above the floor values.³⁷ A buffer is used in this version of PERSEUS that is 1.01 times the density floor. If plasma falls within this density range, then the momentum and current are set to zero, while the energy and density are unchanged. The energy and density are maintained in the positivity preserving limiter.³⁷ The method is capable of handling ≥ 9 orders of magnitude in density variation, from solid density down to the floor value. The Hall-MHD Ohm's law [see Eq. (6)] is solved using the relaxation method described in Ref. 36. The divergence constraint ($\nabla \cdot \mathbf{B} = 0$) is maintained using either divergence cleaning³⁸ or a constrained transport central difference method.³⁹

The simulations have been able to produce helical instabilities solely from Hall physics (i.e., initial helical seeding by the user is not required).^{15,16} In Fig. 1, we present the simulation setup, which includes a plasma liner of uniform initial density and uniform initial temperature, with a low-density coronal plasma layer immediately surrounding the denser liner. The current pulse that drives the simulation is a sine-squared pulse with a rise time of 200 ns and a peak current of 600 kA.

We have attempted to match the conditions of university-scale thin-foil experiments as much as possible. However, due to the computational challenges of properly resolving the ablation of a

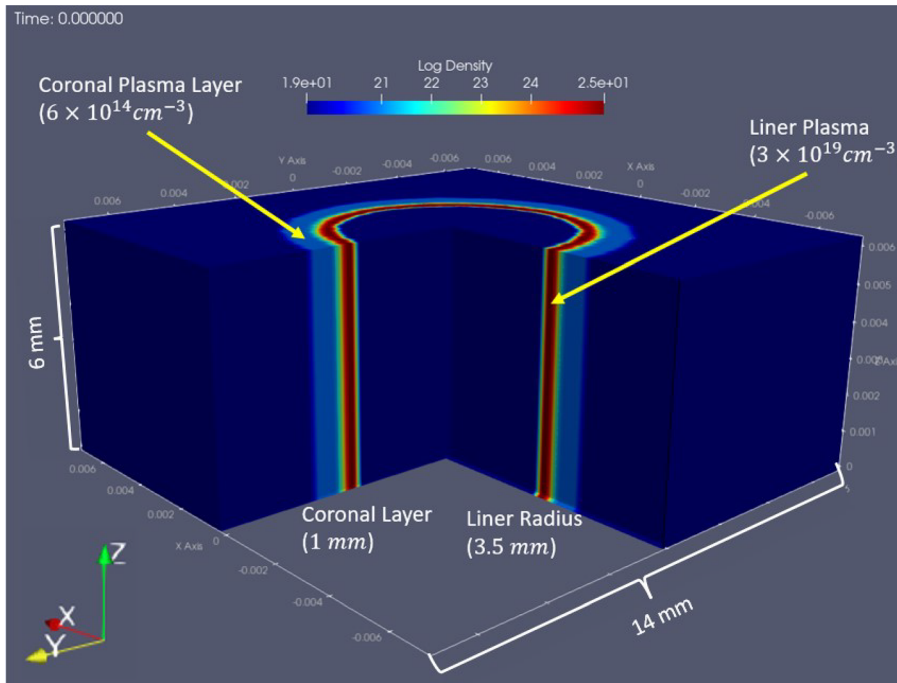


FIG. 1. Initial conditions of the simulation setup that shows the coronal layer ($6 \times 10^{14} \text{ cm}^{-3}$) and the liner plasma ($3 \times 10^{19} \text{ cm}^{-3}$). Two single cell layers between the liner plasma and coronal plasma are included to help step the density down and reduce the sharp density gradient. A uniform 2-T axial magnetic field is applied throughout the simulation volume.

400-nm-thick aluminum foil liner, we have opted to start our simulations 25 ns into the current pulse, at which point the liner has already ablated into a 1-eV liner plasma of 250- μm thickness (though from 0 to 25 ns we allow the fields to evolve while holding the plasma motionless). These post-ablated conditions come from the results of highly resolved HYDRA simulations conducted previously to study the early-time foil ablation process in detail.⁴⁰ We use these post-ablated conditions as the initial conditions for our PERSEUS simulations. These post-ablated initial conditions, as well as the effects of the on-axis plastic support rod (which is necessary to support the thin-foil liners in experiments), are discussed in further detail in Ref. 16.

Immediately surrounding the liner plasma is a low-density coronal plasma layer, initialized with a thickness of 1 mm, a temperature of 5 eV, and a density of $6 \times 10^{14} \text{ cm}^{-3}$, which is $20\times$ the density floor in PERSEUS. Between the coronal layer and the liner plasma are two single cell layers that step the density down from the liner plasma density to the coronal density to prevent numerical effects from sharp density gradients. This coronal layer heats rapidly to a few hundred eV within ~ 10 ns. These plasma parameters lead to the following length and time scales, which show that the coronal plasma is well within a Hall physics regime. The characteristic scale length is $\lambda \sim k^{-1} \sim 0.25 \text{ cm}$, while the collisionless ion skin depth is $l_i = \frac{c}{\omega_{pi}} \sim 10 \text{ cm}$. This is consistent with plasma in a Hall regime. As for the relevant timescales, the characteristic timescale is $\tau \sim \omega^{-1} < 60 \text{ ns}$, the ion gyro period is $\tau_{ci} \sim \Omega_{ci}^{-1} \sim 300 \text{ ns}$, where we must have $\omega > \Omega_{ci} = \frac{ZeB}{m_i c}$ for Hall physics to be relevant. The electron cyclotron period is $\omega_{ce}^{-1} = \left(\frac{eB}{m_e c}\right)^{-1} \sim 0.02 \text{ ns}$ and the collision time is $\nu_e = 2.91 \times 10^{-6} \left(\frac{n_e \ln \Lambda}{T_e^{3/2}}\right) \sim 0.1 \text{ ns}$. These time scales are also consistent with a plasma in a Hall physics dominated regime.

The dynamics of this coronal plasma layer, including its ability to seed helical MRTI, is the subject of this paper.

Each PERSEUS simulation included over 7 million cells, with cell sizes of approximately $62.5 \times 62.5 \times 32 \mu\text{m}^3$, for a total simulation volume of $14 \times 14 \times 6.125 \text{ mm}^3$. The simulations were run on 64 cores on the Great Lakes computing clusters at the University of Michigan. The simulated temporal extent was 250 ns, with time steps on the order of one picosecond. Multiple conductivity models were used, including an approximation to the Lee–More–Desjarlais resistivity model,⁴¹ a Spitzer model, a constant conductivity model, and a zero resistivity model. There is non-negligible numerical resistivity that will allow some penetration of magnetic field into the liner even in the absence of an applied resistivity (this is typical of simulation codes and cannot be easily avoided). It was found that the choice of conductivity model had negligible impact on the Hall instability effects discussed in this paper. Electron velocities are limited through electron inertia; however, this was found to not have significant impact on the behavior of the Hall instability structures. This will be discussed further in Sec. VII. In total, each simulation required upwards of 60 wall-clock hours to run. A random density perturbation of less than 1% was applied to the liner cells and to the corona cells to seed instability growth. A 2-T axial magnetic field was applied throughout the simulation volume initially (and maintained at the radial boundary for the duration of the simulation) to match the previous university-scale pre-magnetized z-pinch experiments.¹⁴

III. HALL-MHD MODEL AND REDUCED MODEL

For a theoretical description of the instability, we derive a local dispersion relation from a reduced Hall-MHD model. This type of analysis is explored in a similar context in Refs. 34 and 35. As discussed previously, PERSEUS includes Hall physics through the Hall

term in the generalized Ohm's law (GOL), which is the third term on the LHS of Eq. (6). The Hall term is necessary to observe the effects discussed in this paper. The Hall-MHD model that will be used for this analysis is as follows:

$$\partial_t n + \nabla \cdot (n\mathbf{u}) = 0, \tag{1}$$

$$\partial_t(\rho\mathbf{u}) + \nabla \cdot (\rho\mathbf{u}\mathbf{u} + p) = \mathbf{J} \times \mathbf{B}, \tag{2}$$

$$\partial_t \varepsilon + \nabla \cdot [\mathbf{u}(\varepsilon + p)] = \mathbf{J} \cdot \mathbf{E}, \tag{3}$$

$$\partial_t \mathbf{B} = -\nabla \times \mathbf{E}, \tag{4}$$

$$\nabla \times \mathbf{B} = \mu_0 \mathbf{J}, \tag{5}$$

$$\mathbf{E} + \mathbf{u} \times \mathbf{B} - \frac{1}{ne} \mathbf{J} \times \mathbf{B} - \eta \mathbf{J} = 0, \tag{6}$$

where $\varepsilon = \frac{1}{2}\rho u^2 + p/(\gamma - 1)$ is the internal energy density, and we have assumed the average ionization is one ($Z = 3$). Equations (1)–(3) are the continuity equations for mass, momentum, and energy, respectively, while Eqs. (4) and (5) are Faraday's and Ampère's laws, respectively. Equation (6) is the generalized Ohm's law with the Hall term included. The variables \mathbf{u} , \mathbf{J} , \mathbf{E} , \mathbf{B} , ρ , n , and p are the fluid velocity, current density, electric field, magnetic field, mass density, number density, and material pressure, respectively.

For theoretical analysis, it is convenient to use a reduced description of the full HMHD equations given by Eqs. (1)–(6). The reduced description of these equations is an asymptotic analysis in which the constant equilibrium axial field B_0 is much larger than either the perturbed axial field or the transverse field, i.e., $B_0 \gg B_z$ and $B_0 \gg B_\perp$. We take $\partial_z \ll \nabla_\perp$, meaning that the perturbations in the axial direction are much smaller than the perturbations in the perpendicular direction, which is consistent with the previous assumption, so that $B_0 \partial_z \sim B_\perp \cdot \nabla_\perp$. The mass velocity is taken to be small but not zero. The pressure perturbations are assumed to be zero, as is the plasma resistivity. We choose to set the resistivity to zero to simplify the derivation. It is also found that the resistivity term does not have an appreciable effect on the simulated growth rate. This is not unexpected due to the low density of the coronal plasma and that it is well within the Hall regime in which the Hall parameter is large. The most familiar application of this scaling leads to the so-called reduced MHD equations, sometimes called the Strauss equations.⁴² The application here is to the Hall-MHD equations in the frequency range between the ion and electron cyclotron frequencies. The high-frequency reduced Hall-MHD model, applicable to plasma motion faster than the ion gyrofrequency and slower than the electron gyrofrequency, consists of the following equations.^{34,35}

$$\partial_t \phi = \frac{1}{n_0 e \mu_0} \left[(\hat{z} \times \nabla \psi) \cdot \nabla \nabla_\perp^2 \psi + B_0 \partial_z \nabla_\perp^2 \psi + B_0 \nabla_\perp^2 \chi + \frac{B_0}{n_0} (\hat{z} \times \nabla n) \cdot \nabla \phi \right], \tag{7}$$

$$\partial_t \psi = \frac{1}{n_0 e \mu_0} [(\hat{z} \times \nabla \psi) \cdot \nabla \phi + B_0 \partial_z \phi], \tag{8}$$

$$\partial_t \chi = -\frac{B_0}{\rho_0 \mu_0} \phi, \tag{9}$$

$$\partial_t n + n_0 \nabla_\perp^2 \chi = 0, \tag{10}$$

where $\phi = \delta B_z$ is the perturbed axial magnetic field, ψ is the magnetic flux function, from which $B_\perp = \hat{z} \times \nabla \psi$, and χ is the velocity

potential. For high frequencies, the velocity is completely compressible such that $\mathbf{u}_\perp = \nabla_\perp \chi$. Equations (7) and (8) are derived from Faraday's law using the Hall-MHD Ohm's law [Eq. (6)]. Equation (9) is the linearized momentum equation for purely compressible modes, and Eq. (10) is the continuity equation for purely compressible motion. The reduced equations are adequate for analyzing the stability about an equilibrium satisfying the stated approximations.

A. Local linear analysis

These equations can be linearized about a slab equilibrium with $B_{0z}(x) = B_0 + \phi_0(x)$, $n_0(x)$ (i.e., a density profile in x), and $B_{0y}(x) = \psi'_0(x)$, where the prime means differentiation with respect to the argument. Additionally, a space-time dependence that is consistent with local analysis can be assumed for the equilibrium and perturbation fields (the terms with δ in the equations below) such that the perturbation fields do not have any dependence on x

$$B_z(x, y, z, t) = B_0 + \phi_0(x) + \delta\phi \exp[i(k_y y + k_z z - \omega t)], \tag{11}$$

$$B_\perp(x, y, z, t) = B_{0y}(x) + \delta\psi \exp[i(k_y y + k_z z - \omega t)], \tag{12}$$

$$\chi(x, y, z, t) = \delta\chi \exp[i(k_y y + k_z z - \omega t)], \tag{13}$$

$$n(x, y, z, t) = n_0(x) + \delta n \exp[i(k_y y + k_z z - \omega t)]. \tag{14}$$

The linearized form of this reduced model is then

$$-i\omega\delta\phi = \frac{1}{n_0 e \mu_0} \left[-ik_y^3 \delta\psi \psi'_0(x) - ik_z k_y^2 B_0 \delta\psi + \psi''_0 + B_0(-k_y^2)\delta\chi + \frac{B_0}{n_0} (n'_0(x) ik_y \delta\phi - ik_y \delta n \phi'_0(x) \delta n) \right], \tag{15}$$

$$-i\omega\delta\psi = \frac{1}{n_0 e \mu_0} [ik_y \delta\psi \phi'_0(x) + ik_y \delta\phi \psi'_0(x) + ik_z B_0 \delta\phi], \tag{16}$$

$$-i\omega\delta\chi = \frac{-B_0}{\rho_0 \mu_0} \delta\phi, \tag{17}$$

$$-i\omega\delta n + n_0(-k_y^2)\delta\chi = 0. \tag{18}$$

Combining and solving Eqs. (15)–(18) gives the local dispersion relation

$$\omega^2 [(\omega - \omega_H)(\omega - \omega_0) - k^2 \sigma^2] - k^2 v_A^2 (\omega^2 - \omega_H^2) = 0, \tag{19}$$

where $v_A^2 = B_0^2 / \rho_0 \mu_0$ (v_A is the Alfvén speed), $k = k_y$, $\omega_0 = k \frac{B_0 n'_0}{n_0^2 e \mu_0}$, $\omega_H = k \frac{\phi'_0}{n_0 e \mu_0}$, $\sigma \equiv [k B_{0y}(x) + \kappa B_0] / (n_0 e \mu_0)$, and $\kappa = k_z$. This gives unstable solutions, requiring ω_H to be non-zero. Note that this instability requires a gradient in the axial magnetic field. The density gradient can work to either make the growth rate larger or smaller depending on whether the density gradient is the same or opposite sign to the magnetic field at the same local radius. This means that the maximal growth rate occurs where the density falls off rapidly ($n'_0 < 0$) and the axial magnetic field gradient has $B'_z < 0$.

Note that this Hall interchange instability differs from other Hall instabilities, such as those explored by Kolberg, Liverts, and Mond.^{43,44} The form of the Hall instability studied in their work manifested as a magnetic field aligned density bunching. The Hall interchange instability explored in this paper produces different effects, namely, the

advection of current and magnetic fields. This will be explored in detail in the following sections.

B. Simulation of the Hall interchange instability

In this subsection, we set up a simple slab equilibrium and test the instability relation in Eq. (19) through a simulation that does not have the added complications of magnetic curvature or of being driven into non-equilibrium by a time-dependent azimuthal magnetic field at the boundary. In this simple simulation, the boundary conditions are conducting at the x boundaries and periodic in y and z . We initialize piece-wise constant and linear profiles in $B(x)$ and $n(x)$. There is no applied resistivity or electron inertia.

We initialize the simulation with B_z , B_y , and a pressure $P = nT$ satisfying force balance $P(x) + \frac{1}{2\mu_0} B^2(x) = \text{const.}$ in a box of dimensions $(L_x, L_y, L_z) = (7.0, 7.0, 6.125)$ mm and $(150, 150, 130)$ cells in the x , y , and z directions. This gives a resolution of $\Delta x = 0.047$ mm. The density profile is $n_0(x) = n_1$ for $x \leq -2\Delta x$, $n_0(x) = n_1(2\Delta x - x)/(4\Delta x)$ for $-2\Delta x < x < 2\Delta x$, and $n_0(x) = n_{\text{floor}}$ for $x \geq 2\Delta x$, where $n_1 = 11n_{\text{floor}}$ at a temperature of 10 eV. The magnetic field is $B_z(x) = 3$ T for $x \leq -2\Delta x$, $B_z(x) = 3(2\Delta x - x)/(4\Delta x)$ T for

$x \geq 2\Delta x$ and $B_z(x) = 2T$ for $x \geq 2\Delta x$. The y -component is determined by pressure balance. There is also a random per cell perturbation in B_y of 0.0005 T.

The results are shown in Figs. 2 and 3. After a brief initial period of transient behavior due to the mismatch of the discretized profiles with continuum force balance, the plasma settles into an equilibrium shown in the rightmost plots of Fig. 2 for the y and z components of the magnetic field and the density. After a few e-folding times, the fastest growing global eigenmode emerges from the random noise. The form of the eigenmode for B_x is the double-peaked red solid curve in Fig. 2, which has been amplified by 50 times for plotting on the same scale as the equilibrium fields. The eigenmode was observed to undergo an e-folding in approximately one nanosecond for a growth rate of $\gamma \approx 10^9 \text{ s}^{-1}$. The result from solving Eq. (19) at the $x = 0$ location gives a real frequency much smaller than the growth rate with $\gamma \approx 0.64 \times 10^9 \text{ s}^{-1}$, which is of the order of the simulation growth rate. We do not consider this discrepancy significant given that the model has assumptions that tend to lower the growth rate from that of the simulation. In particular, the model underestimates ω_H since it does not include the axial electron drift due to the gradient in B_y . If the

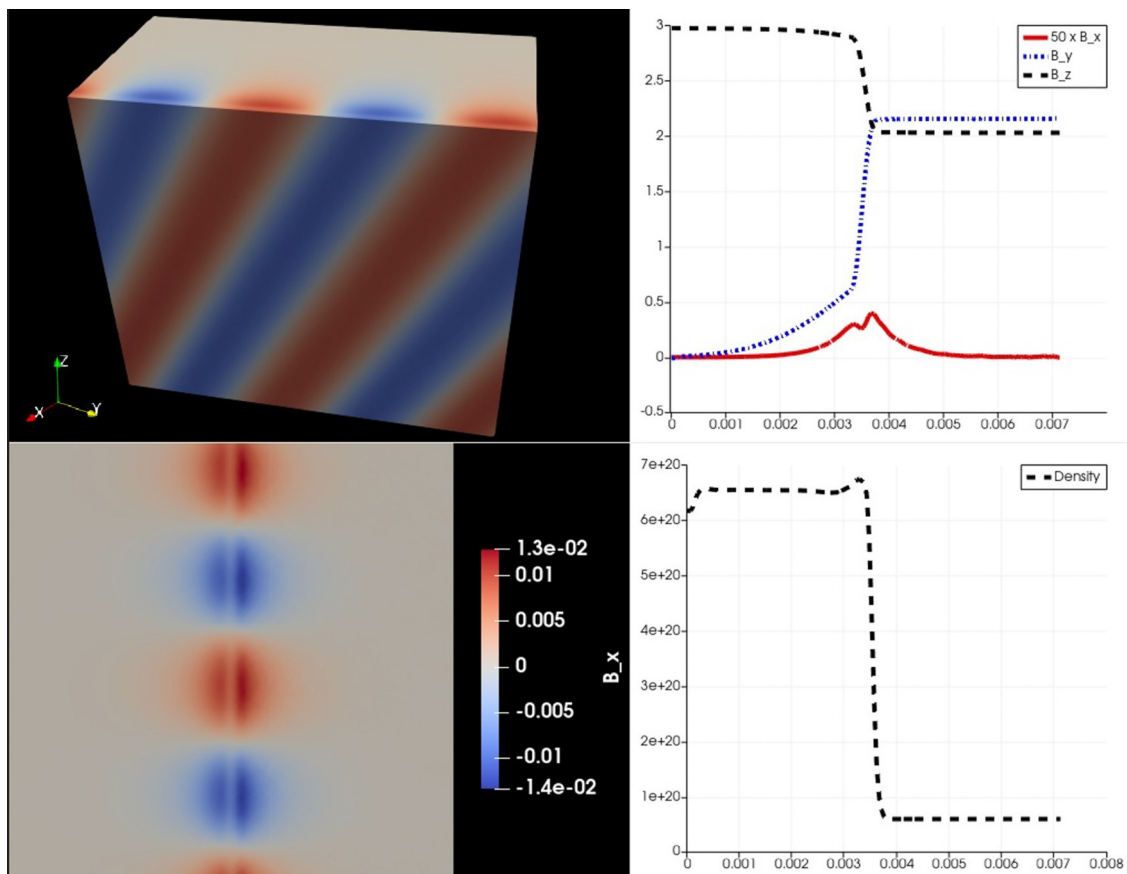


FIG. 2. Plots of the Hall interchange instability in the linear phase at 10 ns. On the left are B_x plots, where the upper plot is B_x on a density isosurface of $3 \times 10^{20} \text{ m}^{-3}$ showing the oblique perturbation approximately parallel to the equilibrium magnetic field. The lower plot is in the x - y plane. The right plots are line-out plots through the peak of B_x . These show the equilibrium $B_z(x)$, $B_y(x)$, and $n_0(x)$. The B_x field is also shown at a magnification of $50\times$ to show the eigenmode structure of the instability. The magnetic field units is tesla and the density is m^{-3} . The simulation domain shown is $7 \times 7 \times 6.125 \text{ mm}^3$.

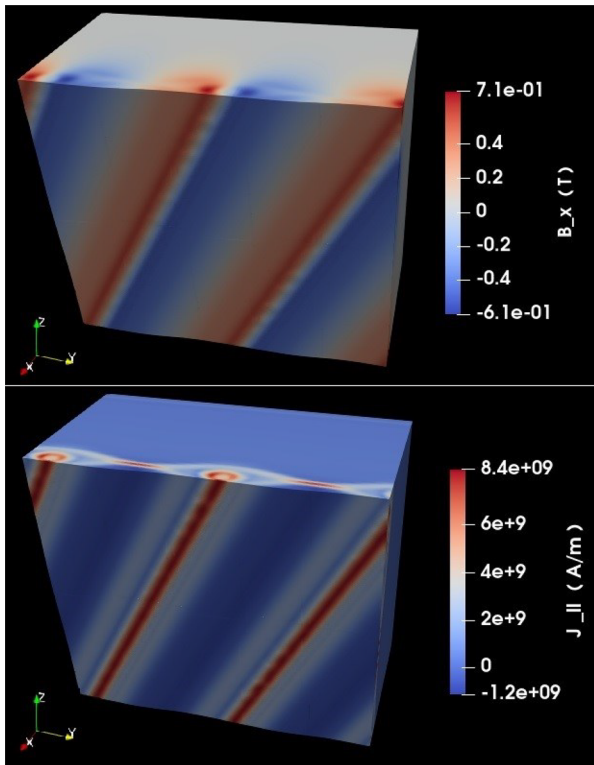


FIG. 3. Plots of B_x and $J_{||}$ in the nonlinear phase. Note that the current has filamented and B_x has a form consistent with the filamented current. The simulation domain shown is $7 \times 7 \times 6.125 \text{ mm}^3$.

B_y gradient drift is included in the calculation of ω_{Hb} , then the growth rate becomes $\gamma \approx 0.95 \times 10^9 \text{ s}^{-1}$, which is much closer to the simulation value. Even with this modification we should not expect strong agreement given the somewhat poor approximation of a localized eigenmode.

In Fig. 3, plots of the parallel current $J_{||}$ and B_x at a late time when nonlinearity is dominant are shown. The current has evolved into cylindrical filaments and the density into ribbon-like filaments (not shown). As we will demonstrate in Sec. IV for the full driven cylindrical liner simulation, the filamented current can penetrate into the dense liner plasma and provide a helical seed for the MRT. No instability was observed for an ideal MHD simulation using the same setup, which is consistent with the known results.

IV. HALL INTERCHANGE INSTABILITY AS A SEED FOR HELICAL MRTI

In an Ideal-MHD context, an interchange instability manifests as magnetic field and plasma trading position, which is localized by magnetic shear and driven by a combination of magnetic curvature and plasma pressure. In the absence of magnetic curvature, the Hall term can drive an interchange instability through electron drifts. With the Hall term, the interchange instability leads to several effects. One of the major effects is that the current is advected into filaments as we noted in the simulations presented in Sec. III. This is driven by magnetic energy release. The result is that helical striations form in the

coronal plasma that surrounds the dense liner plasma. These coronal striations then imprint on the underlying dense liner plasma. In addition, the current is strongly force-free, meaning it is aligned with the magnetic field, and it stays nearly force-free well into the implosion ($>185 \text{ ns}$). The magnetic field also maintains its helicity in large part because of the force-free current being helical as well. The result of the force-free current is that there is a significant amount of azimuthal current, which leads to axial flux amplification. This adds more axial magnetic field helping to maintain the magnetic field helicity, which also leads to seeding of helical MRTI. The axial magnetic field is amplified by a factor of $\sim 8\times$ over the course of the current pulse rise time. The force-free currents can be seen in Fig. 4, at 185 ns into the current pulse, where the magnetic field lines are traced in blue, the current is traced in red, and the dense liner plasma is shown at an iso-density surface (10^{24} m^{-3}) with helical MRTI clearly formed.

The interchange instability strongly influences the flow of currents in the coronal plasma. This leads to a helical perturbation in the azimuthal current that is magnetic field aligned. This perturbation grows quickly and maintains its helical pitch as the magnetic field remains relatively helical due to flux amplification from the azimuthal component of the helical current. The perturbation in the azimuthal component of the current density is shown in Fig. 5.

To demonstrate how the perturbations in the current within the coronal plasma layer lead to seeding of the MRTI structures on the liner plasma, Figs. 6 and 7 are shown, which consist of several slices of the full 3D data at several time steps. In these figures, a transparent iso-density slice of the liner plasma (of density 10^{23} m^{-3}) is overlaid on top of plots of the azimuthal (Fig. 6) and radial (Fig. 7) components of the current density. This shows how the perturbations in the coronal layer embed into the liner plasma and work to seed the wavelength and mode number of the MRTI structures. In Fig. 6, the perturbations in current in the coronal layer embed into the liner plasma, and at 170 ns, where the MRTI structures are outlined on the outer surface of the liner plasma, the current perturbations correlate directly with the MRT instability lobes. The Hall interchange instability drives these

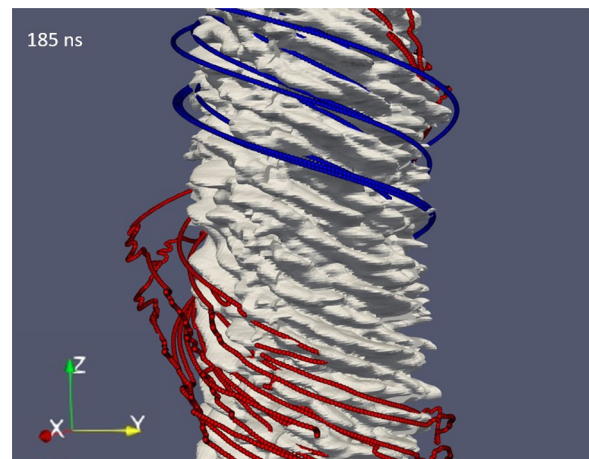


FIG. 4. Helical MRTI forming in the dense liner plasma 185 ns into the current pulse. The iso-density surface shown is for 10^{24} m^{-3} . Magnetic field lines are traced in blue and current density streamlines are traced in red. The plasma column shown is 6 mm tall and has imploded to near stagnation and is $\sim 3 \text{ mm}$ in diameter.

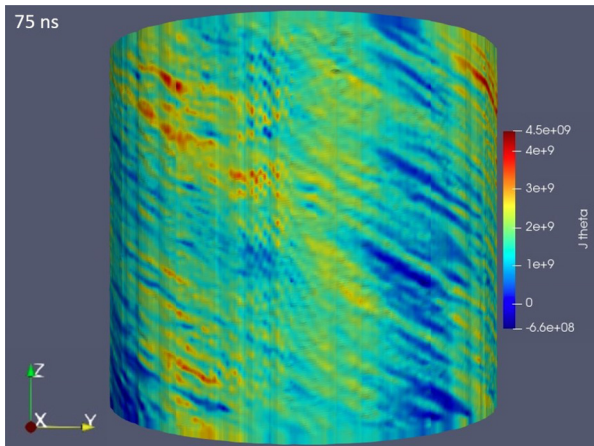


FIG. 5. Helical perturbation in the azimuthal component of the current density, plotted on an iso-density surface (10^{24} m^{-3}) at 75 ns. This highlights one of the perturbation effects of the Hall interchange instability, which leads to helical formations in the current density along the liner’s outer surface. At this time step, the liner shown is 6 mm tall and has not imploded so its radius is still 3.5 mm.

current perturbations early in the coronal plasma current and forms within the first 50 ns of the simulation.

A growth rate for the observed instability is determined by taking an axial line-out through the coronal plasma layer of the azimuthal current bunches and measuring the perturbation amplitude. The growth rate from this analysis is found to be $0.1 \pm 0.02 \text{ ns}^{-1}$. We find that good agreement with the observed result is obtained if we use $B_0 = 2 \text{ T}$, $n_0 = 6 \times 10^{20} \text{ m}^{-3}$, $k = 0.4 \text{ mm}^{-1}$, and a gradient length of $L_g = [B'_z(x)/B_z]^{-1} = 1 \text{ mm}$, the dispersion relation in Eq. (19) gives growth rates of approximately 0.12 ns^{-1} . The reasons for the

significantly lower growth rate for the experimental simulation compared to the slab simulation is due to lower v_A and k and larger L_g for the experimental case. Comparing this with the growth rate γ for MRTI, which for thin-foil liner implosions on the MAIZE facility was found to be $\sim 30 \mu\text{s}^{-1}$ in simulations¹⁶ and $\sim 10 \mu\text{s}^{-1}$ in experiments.¹³ This corresponds to growth times of $\tau = 1/\gamma = 33$ and 100 ns , respectively.

The theoretical growth rate is highly dependent on the initial magnetic field, the coronal plasma density, and the axial wave number. Stronger magnetic field and lower density lead to faster growth rate. A two order of magnitude decrease in density leads to an order of magnitude faster growth rate, while an order of magnitude increase in magnetic field leads to a similar increase in the growth rate. It should be noted that local analysis, which was used to determine the simulated growth rate, often overestimates instability growth rates. A plot of this growth rate is shown in Fig. 8. The error bars are determined by one standard deviation in the instability amplitudes at each time step. Note that there is a steep drop off in the growth rate at $>75 \text{ ns}$. This is likely due to nonlinear saturation of the interchange instability or to other slower growing instabilities like MRTI becoming dominant and disrupting the interchange instability.

In Fig. 9, the instability’s axial wave number is plotted. This wave number evolves very quickly to an almost constant value, once the plasma is allowed to move during post-ablation times (i.e., $>25 \text{ ns}$ into the current pulse, as discussed in Sec. II). This wave number remains relatively constant while the Hall interchange instability is still the dominant instability effect.

Note that for this growth rate analysis, the resistivity in the simulation was set to zero throughout. This was done due to the fact that the theoretical analysis and theoretical growth rate were determined assuming zero resistivity. It was found that changing the conductivity model from a coupled Lee–More–Desjarlais and Spitzer model to a

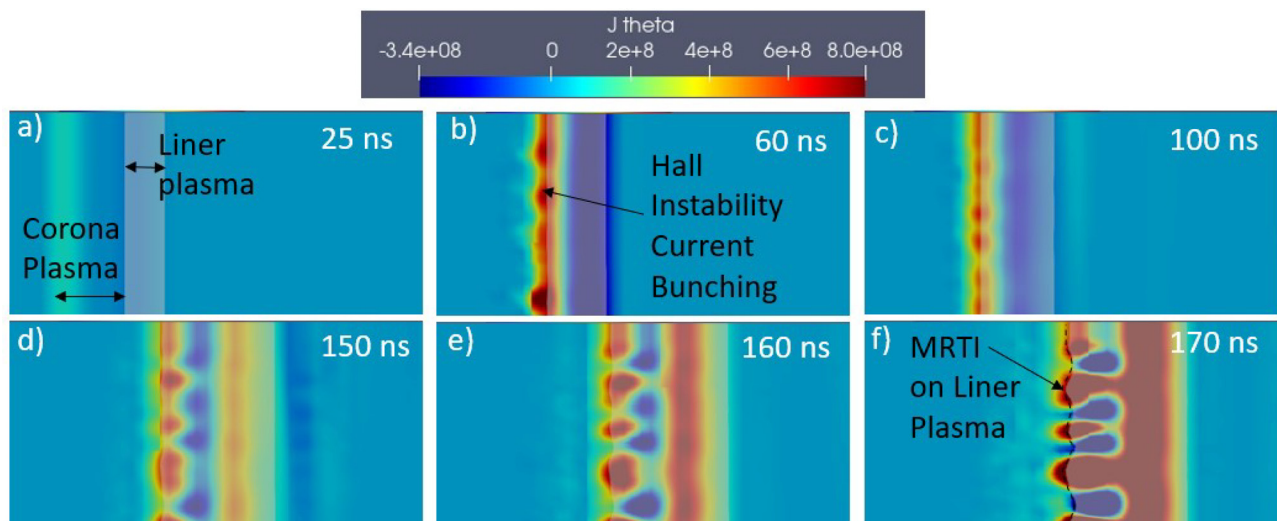


FIG. 6. (a)–(f) Perturbation in the azimuthal component of the current density, plotted with an iso-density surface slice of the liner plasma (10^{23} m^{-3}) at six time steps to show the process of the perturbations forming in the coronal layer and embedding into the dense liner plasma. These images are in the x - z plane with the cylindrical axis of symmetry being the right edge of each image, while the outer simulation boundary is the left edge of the images. The section of the liner plasma shown is only 2 mm tall and the image covers 5 mm in the x -axis.

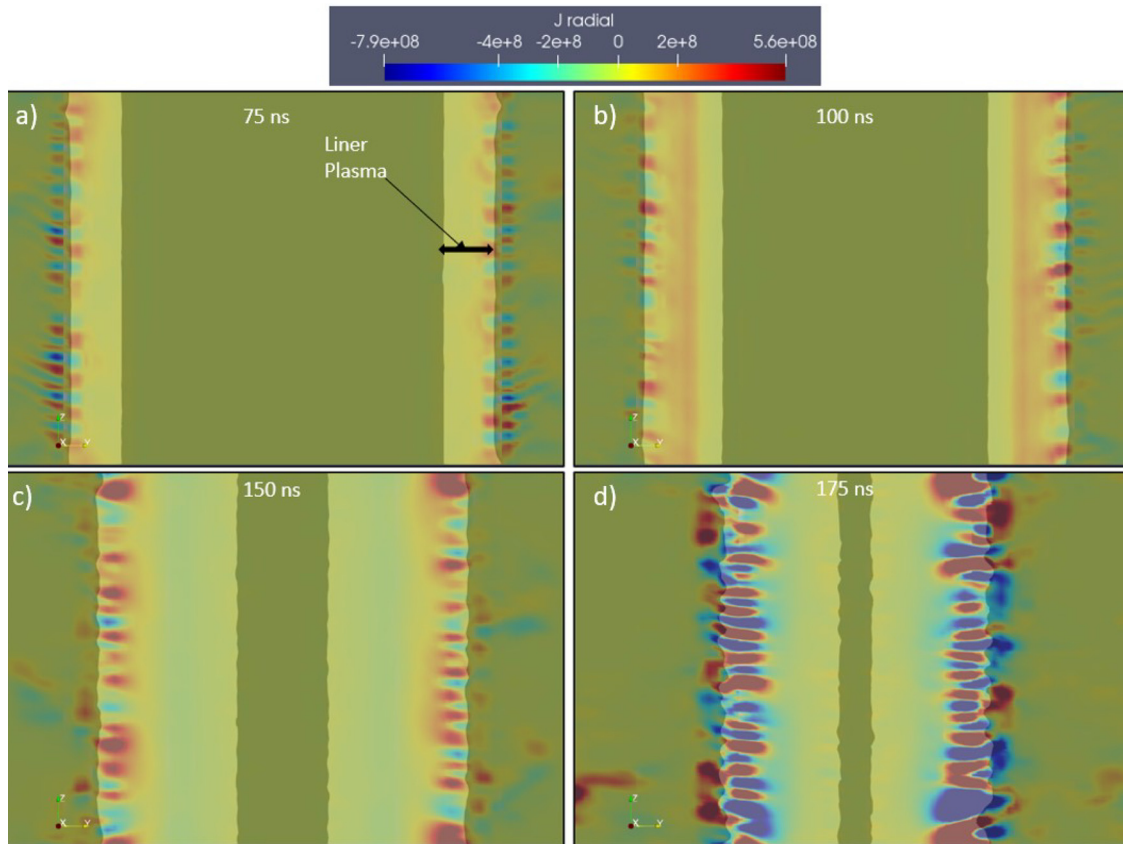


FIG. 7. (a)–(d) Perturbation in the radial component of current density, plotted on a 2D slice from the simulation volume. Overlaid are semi-transparent iso-density surfaces of the dense liner plasma (10^{23} m^{-3}). Images from four different times are presented to illustrate the process of the perturbations forming in the coronal layer and extending into the dense liner plasma. The dimensions of each image are 6 mm tall by 8 mm and show the y – z plane.

constant value of zero resistivity had little effect on the Hall instability dynamics.

Electron inertia terms were included in some simulations to provide a limiting mechanism for electron velocities, but it was found that the inertia terms had no discernible effect on the Hall instability dynamics compared to a limiting method using a static limiter term. In either case, the electron velocities never exceeded the speed of light.

V. BOUNDARY CONDITION EFFECTS

An important factor that determines the dynamics of the coronal layer, and therefore, the dynamics of the liner implosion, is the choice of boundary condition on the upper and lower z boundaries. We consider two boundary conditions in this work, namely, periodic and open boundaries.

Periodic boundary conditions lead to reduced Hall instability effects as compared to an open boundary condition. This is due in part to the periodic boundary condition leading to the compression of the coronal layer onto the liner's outer surface faster than what is seen in an open boundary simulation. This is in large part due to periodic boundary conditions on the lower and upper z boundaries not allowing azimuthal flux to leave through the boundary. This prevents several effects

that would lead to axial flux amplification, which in turn leads to the coronal layer being compressed by $\mathbf{J} \times \mathbf{B}$ forces within the first 50 ns of the simulation. The consequence is that Hall effects are not able to establish in the coronal layer before its compression and, therefore, do not have the requisite time to seed helical MRTI in the liner plasma.

When an open boundary condition is implemented on the axial boundaries, azimuthal flux (and, therefore, EM energy) is able to leave the simulation domain by outflow, which allows for the amplification of axial magnetic flux. This effect was studied in 2D by Seyler in the context of gas-puff z -pinches.⁴⁵ In those gas-puff simulations, it was found that the choice of boundary condition was imperative to producing an increase in B_z due to use of a Poynting outflow boundary condition. The outflowing EM energy increased the Hall driven effects, which led to force-free current shells producing additional axial magnetic flux. The driving factor of this effect is the conductivity tensor derived from inverting the GOL: $\mathbf{J} = \bar{\sigma} \cdot (\mathbf{E} + \mathbf{u} \times \mathbf{B})$. This is an effect of including the Hall term. The parallel term (with respect to the magnetic field) in the conductivity tensor is the most conducting, and therefore, it leads to currents flowing along magnetic field lines. For strongly magnetized electrons, the total current, which is generally force free, is approximately:

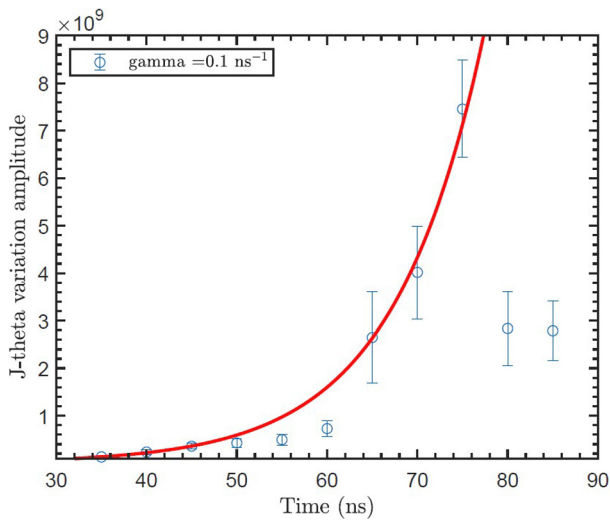


FIG. 8. Plot of the azimuthal current density perturbation amplitude growth rate. The amplitude was taken by an axial line-out through the coronal plasma subject to the Hall interchange instability. The growth rate found from this analysis compares very closely to the growth rate predicted by theory. The error bars are determined from one standard deviation in the perturbation amplitude.

$$\mathbf{J} = \mathbf{B} \frac{B_z E_z}{B^2 \eta}. \quad (20)$$

More generally this current is $\mathbf{J} = \hat{b} \hat{b} \cdot \mathbf{E} / \eta$, where \hat{b} is the unit vector in the direction of the magnetic field. If this current exists in a small sheath region, then outside this current sheath, there will be only azimuthal field, and inside this sheath, there will be only axial field. This is indeed what was observed in Ref. 45. A consequence of the loss of azimuthal flux and increase in axial flux was a reduction in the

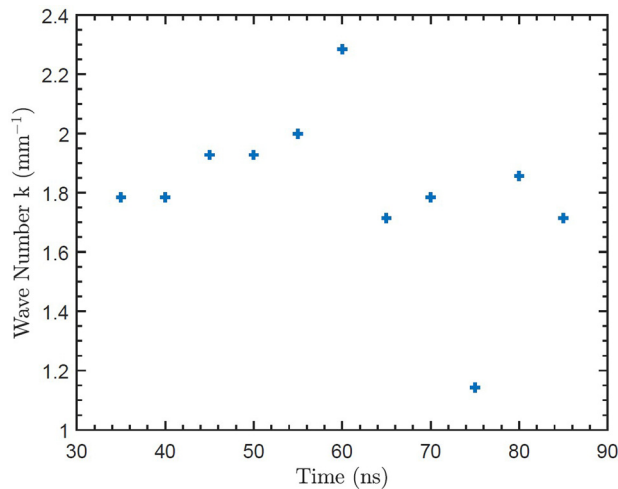


FIG. 9. Plot of the axial wave number of the perturbation in the azimuthal current density. The wave number is set within a few nanoseconds of the simulation and remains fairly constant throughout the period when the interchange instability is still the most important instability (≈ 80 ns).

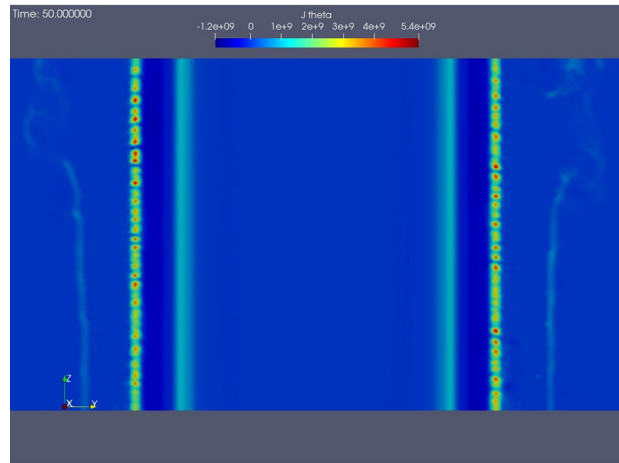


FIG. 10. Plot of a 2D slice of J_θ from a 3D simulation of a thin-foil z-pinch with open outflow boundary conditions on the upper and lower z boundaries at 50 ns. The Hall instability bunching of J_θ in the coronal layer is evident. Also evident is the filament of J_θ discussed in the gas-puff z-pinch simulations of Ref. 45. The simulation space shown in this image is 6 mm tall by 14 mm in the y - z plane.

implosion of the gas puff due to the increase in axial magnetic pressure. This effect was only seen when the Hall term was included in the GOL. The hallmark of this effect was the establishment of a long-lived shell of current in the low density plasma surrounding the gas-puff at large radii. For the 3D thin-foil simulations presented here, a similar current effect is observed early in the simulation. This current effect is shown in Fig. 10, where the azimuthal current component is plotted on a 2D slice of the 3D data at 50 ns. One difference between the 3D thin-foil liner simulations presented here in this paper and the 2D gas puff simulations presented in Ref. 45 is that the current filament in this work does not have the same stability as the one observed in the gas-puff simulations. In Fig. 10, at the top of the simulation, the filament is already being dispersed at 50 ns. It is not observed in the thin-foil simulation beyond ~ 80 ns. This difference is due to the use of the Poynting outflow boundary condition in the gas-puff simulations of Ref. 45, which leads to more outflow of the azimuthal flux as compared with the outflow boundary conditions used here. A Poynting outflow boundary condition (BC) applies a gradient at the boundary. This draws more EM energy out of the simulation volume, as compared to that drawn by an outflow BC that does not have the gradient applied (but which still allows EM energy to leave the simulation volume). The thin-foil simulations shown here implemented an outflow axial boundary condition with no gradient applied. The correct axial boundary condition for the thin-foil z-pinch liner is difficult to know and would require careful experimental work. For example, experiments could be conducted with different electrode options, such as an anode mesh (as in typical gas-puff experiments⁴⁵) a solid anode close to the top of the imploding liner (as in MagLIF experiments³) or a solid anode far above the top of the imploding liner (as in thin-foil experiments on MAIZE¹⁴).

VI. COMPARISON OF HALL-MHD AND MHD

One of the capabilities of PERSEUS is that it is easy to switch Hall physics on and off. This allows for direct comparisons of

simulations of the coronal layer with and without Hall physics included. This section presents a series of comparisons to demonstrate that Hall physics is necessary to see the effects discussed in this paper. Note that the only difference in the two simulations is whether the Hall term is included. All other aspects of the simulations are the same, including the density floor.

In Fig. 11, a series of comparison images of the azimuthal component of the current density at 75 and 100 ns is presented. The first four images [Figs. 11(a)–11(d)] are 2D slices from full 3D simulations, which show that when Hall physics is included, the characteristic perturbations in azimuthal current are present, and when Hall physics is omitted, these perturbations are not present. Figures 11(a) and 11(b) show a side-on view of the azimuthal current density in the coronal layer at 75 ns. The liner plasma is represented as a transparent gray iso-density slice (10^{24} m^{-3}), similar to Figs. 6 and 7. At this time step, the liner plasma has not begun to implode. In the MHD case [Fig. 11(b)], the azimuthal current lacks the regular bunching in the coronal layer that is the result of the Hall instability. By contrast, this regular bunching in the coronal layer is seen in the simulations that include the Hall term in the generalized Ohm's law [Fig. 11(a)].

To show how the Hall interchange instability affects the current density on the surface of the liner plasma, Figs. 11(e) and 11(f) are presented, both of which show iso-density surfaces of 10^{24} m^{-3} and azimuthal current density at 100 ns. In the MHD case [Fig. 11(f)], there is no pattern to the azimuthal current density, while in the case with Hall physics [Fig. 11(e)], there is a clear regular helical pattern on the liner's outer-surface. When Hall physics is included, the Hall instability in the coronal layer leads to this helical pattern on the liner's outer surface, which can then provide a seed for the helical MRTI discussed throughout this paper.

Another important aspect to the interchange instability (driven by the Hall term) is its adherence to a helical force-free configuration of the current and magnetic field. To demonstrate this, Fig. 12 is presented, with magnetic field and current density streamlines traced around the liner at a time of 100 ns into the current pulse. As discussed, when Hall physics is included, current filaments are produced and are seen in the current traces of Fig. 12, which shows a switch-back like feature. The switch-back feature is a consequence of the streamline tracing interpolator trying to properly capture the filaments. This feature is not seen in simulations that do not include Hall physics.

Due to the lack of Hall instability effects in the MHD case, helical MRTI structures are not observed. The MRT instability is azimuthally correlated, as is the magnetic field, after ~ 160 ns. When Hall physics is included, the MRTI structures are very helical, as seen in Fig. 4. This dependence on including Hall physics to produce helical MRTI structures was also seen in our previous simulations of thin-foil liner z-pinches.¹⁶

VII. DISCUSSION

As discussed in Sec. III, the Hall interchange instability is not dependent on the resistive term in the GOL. This means that the conductivity model is relatively unimportant to the development of the instability perturbations observed in the coronal plasma layer. This has been confirmed by using several different conductivity models. These efforts found no qualitative differences in the Hall instability effects.

Additionally, the electron inertia terms are unimportant for the development and dynamics of the Hall instability. This was determined by running PERSEUS simulations with electron velocities limited by either an artificial limiting term or by the inclusion of the electron inertia terms. The effects in both cases were the same. That said, it is important to limit the electron velocities so that they do not exceed the speed of light; otherwise, nonphysical instability structures and effects takeover.

Simulations were also run where the starting density of the coronal layer was increased by a factor of 10, and the Hall effects were not seen. This is due to the fact that the Hall term in the GOL has an inverse relation to density; thus, the Hall term has its strongest effect (relative to resistive effects) in low-density plasmas. To observe the effects described in this paper, it is necessary to achieve as low of a density floor as possible. PERSEUS's capabilities in modeling 9–10 orders of magnitude in density allows it to achieve a low enough density floor for the Hall effects to occur within the coronal plasma layer. PERSEUS simulations were run in which the coronal plasma layer was non-existent or was compressed against the liner within the first few time steps. In these simulations, the Hall instability effects were not present, as there was no coronal plasma layer. As a result, the liner plasma did not produce helical MRTI as it imploded; instead, the MRTI structures were azimuthal. A key aspect that determines the preservation of the coronal layer is the choice of the fast wave speed within the flux routine of the code. In the version of PERSEUS used in this study, a flux solver is implemented as described by Batten *et al.*,⁴⁶ where the fast wave speed was set to be the Alfvén speed plus the ion sound speed. If this value was set to be just the ion sound speed, the coronal layer was not preserved. The choice of the fast wave speed determines if the outer surface of the liner plasma has a pseudo-ablation effect that allows the coronal layer to persist around the liner plasma. This phenomenon is not exactly physical in the code, but it captures the effects of the coronal plasma that are known to occur in experiment.³³ Modeling the true physical mechanisms involved with the coronal plasma formation is beyond the capabilities of PERSEUS and may require kinetic modeling (e.g., to model electrical breakdown and surface flashover). Additionally, to model the ablation physics properly would require very detailed conductivity and equation of state models as well as extremely high grid resolution to properly describe the 400-nm-thick foil. That said, the Hall effects that then occur in the coronal plasma layer are well within the scope of PERSEUS' capabilities.

An instability in the same growth rate range as the Hall instability, which should be discussed here, is the lower-hybrid drift instability (LHDI),^{47–49} which gives rise to robust anomalous transport effects when the perpendicular electron drift velocity is near or exceeds the thermal ion speed [i.e., $j_{\perp}/(en_e v_{th}) \geq 1$]. In the simulations presented, this ratio is found to be of order one in the coronal plasma. In the coronal plasma just outside of the liner plasma, which produces the instability effects discussed in this paper, the ratio of perpendicular electron drift velocity to ion thermal speed is somewhat lower suggesting that the Hall instability is still the dominant effect since the Hall instability can be driven solely by the parallel current. We are currently working on an implementation of anomalous resistivity in PERSEUS to further explore the effect of LHDI; however, the version of PERSEUS used in this study was not capable of addressing the specifics of the LHDI, and a thorough detailed study is beyond the scope of this paper and must be left to the future work.

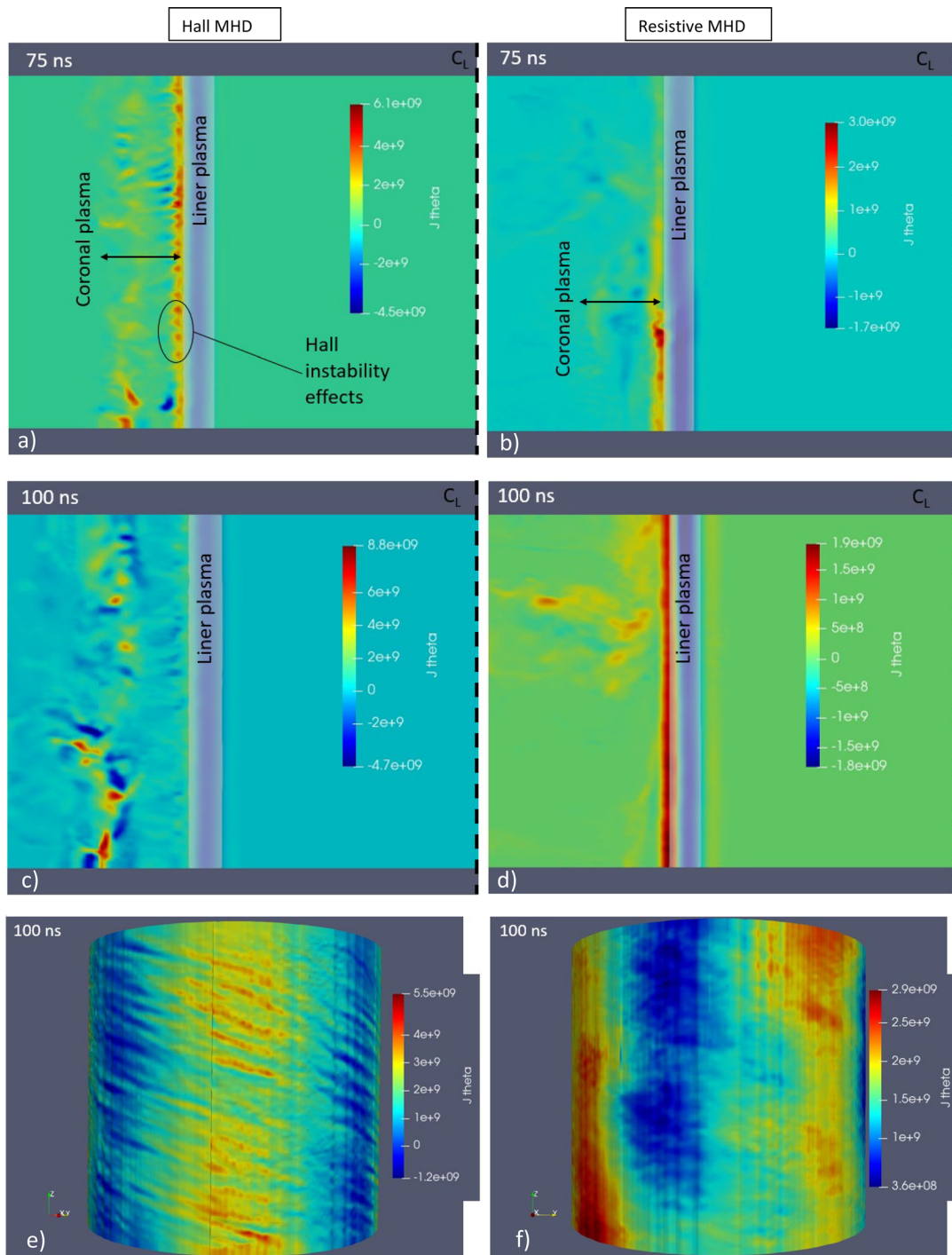


FIG. 11. (a)–(d) Plots of the azimuthal current density from 2D slices ($6 \times 6 \text{ mm}^2$) of the full 3D simulations in the y – z plane at 75 and 100 ns with Hall physics included (a) and (c) and with Hall physics omitted (b) and (d). These images also have a partially transparent gray iso-density slice (10^{24} m^{-3}) overlaid to show the liner plasma for reference. The cylindrical axis of symmetry (centerline) is the rightmost edge of these first four images. The images that lack Hall physics (b) and (d) show that current density bunching (a Hall instability effect) does not occur. When Hall physics is included (a) and (c), the perturbations in the current density within the coronal plasma layer are evident. The disparity between Hall MHD and MHD simulations is further highlighted in images (e) and (f), which show isodensity surfaces of 10^{24} m^{-3} (the liner is 6 mm tall by ~ 3.5 mm in radius) from 3D simulations with Hall physics included and omitted, respectively. In (e), the helical striations driven by the Hall interchange instability are present, while they are not present in (f) due to the lack of Hall physics.

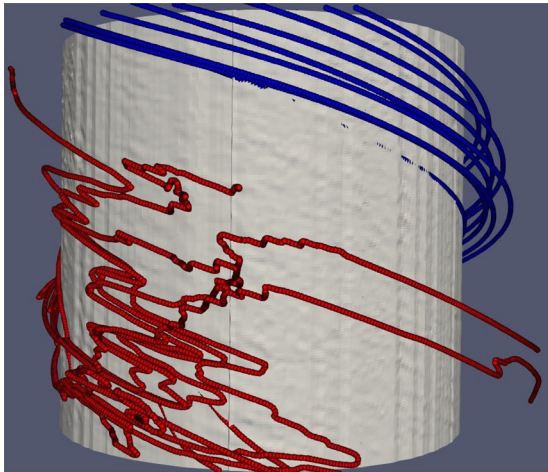


FIG. 12. Plot from a simulation including Hall MHD of the liner plasma at an isodensity surface of 10^{23} m^{-3} with magnetic field traced in blue and current density traced in red at 100 ns. The current is helical and generally force-free due to effects from the Hall term. Note also that the current traces have a switch-back like feature, which is due to the current filaments created by the Hall instability. The liner is 6 mm tall by ~ 3.5 mm in radius at this time.

VIII. SUMMARY, CONCLUSIONS, AND FUTURE WORK

In this paper, we have demonstrated a new, independent seeding mechanism for helical MRTI in thin-foil liner z-pinch implosions, which is driven by Hall physics effects. Several explanations for seeding mechanisms have been proposed for the thick-walled liner z-pinch implosions studied on the Z facility at Sandia National Laboratories. However, many of these explanations are not applicable to the university-scale (~ 1 -MA) thin-foil liners that were studied for this work. For example, it has been proposed^{15,29} that the helical MRTI observed in MagLIF implosions on Z is the result of low-density plasma being produced in the anode–cathode gaps of the 20-MA Z-machine. Prior to the implosion of the liner, this low-density plasma in the anode–cathode gap implodes onto the liner’s outer surface. Embedded in this low-density plasma is the pre-imposed B_z field. Thus, the B_z flux is compressed up against the liner’s outer surface, thereby amplifying B_z and increasing the ratio of B_z/B_θ at the liner’s outer surface. However, recent university experiments have found that very little plasma is produced in the anode–cathode gaps of smaller, 1-MA machines without doing something very deliberate to produce the plasma.³¹ Yet, thin-foil liner z-pinch implosions on MAIZE still develop helical instabilities.¹⁴ Thus, another mechanism must be responsible for the helical MRTI, at least for thin-foil liner implosions on smaller, 1-MA machines.

A second seeding mechanism that is thought to play a significant role in the seeding of helical MRTI in MagLIF implosions on Z is the electro-thermal instability (ETI). However, this instability seeding mechanism is not accounted for in the PERSEUS simulations presented herein, because PERSEUS lacks the requisite material and conductivity models. Thus, in these PERSEUS simulations, it is the Hall instability and Hall effects that produce the helical MRTI structures observed.

We have shown that a Hall interchange instability in the low-density coronal plasma that surrounds a thin-foil liner during an electrical discharge is responsible for several mechanisms that lead to the

seeding of helical MRTI. These mechanisms include current advection, magnetic field effects, and a prolonged force-free configuration of the current and magnetic field. We have also derived a new analytic result for the Hall interchange instability, based on a reduced Hall-MHD model, which shows good agreement with the simulated liner results. It was found that the growth rate for the Hall interchange instability, derived from our analytic work ($0.12 \pm 0.05 \text{ ns}^{-1}$), matched the growth rate found in simulation ($0.1 \pm 0.02 \text{ ns}^{-1}$) quite closely. It has also been shown that Hall physics is required to produce these effects.

Detailed experimental work will be needed to determine the interplay of the Hall interchange instability and other effects in the seeding of helical MRTI. In future simulations and experiments, it will be important to understand how the coronal plasma layer is formed and maintained. Along with this, electro-thermal instability effects are beyond the current capabilities of PERSEUS, as it is extremely difficult to properly resolve the phase transitions of the thin aluminum foil from solid metal to low-density plasma. Doing so will require more robust conductivity models and/or kinetic models.

ACKNOWLEDGMENTS

The authors would like to thank all those at Cornell University who worked to bring PERSEUS capabilities to the University of Michigan.

This research was supported by the NNSA Stewardship Sciences Academic Programs under DOE Cooperative Agreement No. DE-NA0003764.

Sandia National Laboratories is a multimission laboratory managed and operated by National Technology & Engineering Solutions of Sandia, LLC, a wholly owned subsidiary of Honeywell International Inc., for the U.S. Department of Energy’s National Nuclear Security Administration under contract DE-NA0003525. This paper describes objective technical results and analysis. Any subjective views or opinions that might be expressed in the paper do not necessarily represent the views of the U.S. Department of Energy or the United States Government. This paper is SAND2022-16235 J.

AUTHOR DECLARATIONS

Conflict of Interest

The authors have no conflicts to disclose.

Author Contributions

Jeffrey M Woolstrum: Conceptualization (equal); Formal analysis (equal); Investigation (equal); Methodology (equal); Writing – original draft (equal). **Charles E. Seyler:** Conceptualization (equal); Formal analysis (equal); Investigation (equal); Methodology (equal); Validation (equal); Writing – original draft (equal). **Ryan McBride:** Conceptualization (equal); Funding acquisition (equal); Resources (equal); Supervision (equal); Writing – review & editing (equal).

DATA AVAILABILITY

The data that support the findings of this study are available from the corresponding author upon reasonable request.

REFERENCES

- ¹S. A. Slutz, M. C. Herrmann, R. A. Vesey, A. B. Sefkow, D. B. Sinars, D. C. Rovang, K. J. Peterson, and M. E. Cuneo, *Phys. Plasmas* **17**, 056303 (2010).
- ²M. R. Gomez, S. A. Slutz, A. B. Sefkow, D. B. Sinars, K. D. Hahn, S. B. Hansen, E. C. Harding, P. F. Knapp, P. F. Schmit, C. A. Jennings, T. J. Awe, M. Geissel, D. C. Rovang, G. A. Chandler, G. W. Cooper, M. E. Cuneo, A. J. Harvey-Thompson, M. C. Herrmann, M. H. Hess, O. Johns, D. C. Lamppa, M. R. Martin, R. D. McBride, K. J. Peterson, J. L. Porter, G. K. Robertson, G. A. Rochau, C. L. Ruiz, M. E. Savage, I. C. Smith, W. A. Stygar, and R. A. Vesey, *Phys. Rev. Lett.* **113**, 155003 (2014).
- ³D. B. Sinars, M. A. Sweeney, C. S. Alexander, D. J. Ampleford, T. Ao, J. P. Apruzese, C. Aragon, D. J. Armstrong, K. N. Austin, T. J. Awe, A. D. Baczewski, J. E. Bailey, K. L. Baker, C. R. Ball, H. T. Barclay, S. Beatty, K. Beckwith, K. S. Bell, J. F. Benage, N. L. Bennett, K. Blaha, D. E. Bliss, J. Boerner, C. J. Bourdon, B. A. Branch, J. L. Brown, E. M. Campbell, R. B. Campbell, D. G. Chacon, G. A. Chandler, K. Chandler, P. J. Christenson, M. D. Christon, E. B. Christner, R. C. Clay, K. R. Cochrane, A. P. Colombo, B. M. Cook, C. A. Coverdale, M. E. Cuneo, J. S. Custer, A. Dasgupta, J.-P. Davis, M. P. Desjarlais, D. H. Dolan, J. D. Douglass, G. S. Dunham, S. Duwal, A. D. Edens, M. J. Edwards, E. G. Evstatiev, B. G. Farfan, J. R. Fein, E. S. Field, J. A. Fisher, T. M. Flanagan, D. G. Flicker, M. D. Furnish, B. R. Galloway, P. D. Gard, T. A. Gardiner, M. Geissel, J. L. Giuliani, M. E. Glinisky, M. R. Gomez, T. Gomez, G. P. Grim, K. D. Hahn, T. A. Haill, N. D. Hamlin, J. H. Hammer, S. B. Hansen, H. L. Hanshaw, E. C. Harding, A. J. Harvey-Thompson, D. Headley, M. C. Herrmann, M. H. Hess, C. Highstrete, O. A. Hurricane, B. T. Hutsel, C. A. Jennings, O. M. Johns, D. Johnson, M. D. Johnson, B. M. Jones, M. C. Jones, P. A. Jones, P. E. Kalita, R. J. Kamm, J. W. Kellogg, M. L. Kiefer, M. W. Kimmel, P. F. Knapp, M. D. Knudson, A. Kreft, G. R. Laity, P. W. Lake, D. C. Lamppa, W. L. Langston, J. S. Lash, K. R. LeChien, J. J. Leckbee, R. J. Leeper, G. T. Leifeste, R. W. Lemke, W. Lewis, S. A. Lewis, G. P. Loisel, Q. M. Looker, A. J. Lopez, D. J. Lucero, S. A. MacLaren, R. J. Magyar, M. A. Mangan, M. R. Martin, T. R. Mattsson, M. K. Matzen, A. J. Maurer, M. G. Mazarakis, R. D. McBride, H. S. McLean, C. A. McCoy, G. R. McKee, J. L. McKenney, A. R. Miles, J. A. Mills, M. D. Mitchell, N. W. Moore, C. E. Myers, T. Nagayama, G. Naton, A. C. Owen, S. Patel, K. J. Peterson, T. D. Pointon, J. L. Porter, A. J. Porwitzky, S. Radovich, K. S. Raman, P. K. Rambo, W. D. Reinhart, G. K. Robertson, G. A. Rochau, S. Root, D. V. Rose, D. C. Rovang, C. L. Ruiz, D. E. Ruiz, D. Sandoval, M. E. Savage, M. E. Scefird, M. A. Schaeuble, P. F. Schmit, M. S. Schollmeier, J. Schwarz, C. T. Seagle, A. B. Sefkow, D. B. Seidel, G. A. Shipley, J. Shores, L. Shulenburg, S. C. Simpson, S. A. Slutz, I. C. Smith, C. S. Spears, P. E. Specht, M. J. Speir, D. C. Spencer, P. T. Springer, A. M. Steiner, B. S. Stoltzfus, W. A. Stygar, J. Ward Thornhill, J. A. Torres, J. P. Townsend, C. Tyler, R. A. Vesey, P. E. Wakeland, T. J. Webb, E. A. Weinbrecht, M. R. Weis, D. R. Welch, J. L. Wise, M. Wu, D. A. Yager-Elorriaga, A. Yu, and E. P. Yu, *Phys. Plasmas* **27**, 070501 (2020).
- ⁴D. D. Ryutov, M. S. Derzon, and M. K. Matzen, *Rev. Mod. Phys.* **72**, 167 (2000).
- ⁵R. D. McBride, W. A. Stygar, M. E. Cuneo, D. B. Sinars, M. G. Mazarakis, J. J. Leckbee, M. E. Savage, B. T. Hutsel, J. D. Douglass, M. L. Kiefer, B. V. Oliver, G. R. Laity, M. R. Gomez, D. A. Yager-Elorriaga, S. G. Patel, B. M. Kovalchuk, A. A. Kim, P. A. Gourdain, S. N. Bland, S. Portillo, S. C. Bott-Suzuki, F. N. Beg, Y. Maron, R. B. Spielman, D. V. Rose, D. R. Welch, J. C. Zier, J. W. Schumer, J. B. Greenly, A. M. Covington, A. M. Steiner, P. C. Campbell, S. M. Miller, J. M. Woolstrum, N. B. Ramey, A. P. Shah, B. J. Sporer, N. M. Jordan, Y. Y. Lau, and R. M. Gilgenbach, *IEEE Trans. Plasma Sci.* **46**, 3928 (2018).
- ⁶E. G. Harris, *Phys. Fluids* **5**, 1057 (1962).
- ⁷D. Colombant, W. Manheimer, and E. Ott, *Phys. Rev. Lett.* **53**, 446 (1984).
- ⁸T. J. Awe, R. D. McBride, C. A. Jennings, D. C. Lamppa, M. R. Martin, D. C. Rovang, S. A. Slutz, M. E. Cuneo, A. C. Owen, D. B. Sinars, K. Tomlinson, M. R. Gomez, S. B. Hansen, M. C. Herrmann, J. L. McKenney, C. Nakhleh, G. K. Robertson, G. A. Rochau, M. E. Savage, D. G. Schroen, and W. A. Stygar, *Phys. Rev. Lett.* **111**, 235005 (2013).
- ⁹T. J. Awe, C. A. Jennings, R. D. McBride, M. E. Cuneo, D. C. Lamppa, M. R. Martin, D. C. Rovang, D. B. Sinars, S. A. Slutz, A. C. Owen, K. Tomlinson, M. R. Gomez, S. B. Hansen, M. C. Herrmann, M. C. Jones, J. L. McKenney, G. K. Robertson, G. A. Rochau, M. E. Savage, D. G. Schroen, and W. A. Stygar, *Phys. Plasmas* **21**, 056303 (2014).
- ¹⁰A. G. Roussikh, A. S. Zhigalin, V. I. Oreshkin, V. Frolova, A. L. Velikovich, G. Y. Yushkov, and R. B. Baksht, *Phys. Plasmas* **23**, 063502 (2016).
- ¹¹D. A. Yager-Elorriaga, P. Zhang, A. M. Steiner, N. M. Jordan, P. C. Campbell, Y. Y. Lau, and R. M. Gilgenbach, *Phys. Plasmas* **23**, 124502 (2016).
- ¹²T. J. Awe, K. J. Peterson, E. P. Yu, R. D. McBride, D. B. Sinars, M. R. Gomez, C. A. Jennings, M. R. Martin, S. E. Rosenthal, D. G. Schroen, A. B. Sefkow, S. A. Slutz, K. Tomlinson, and R. A. Vesey, *Phys. Rev. Lett.* **116**, 065001 (2016).
- ¹³D. A. Yager-Elorriaga, P. Zhang, A. M. Steiner, N. M. Jordan, Y. Y. Lau, and R. M. Gilgenbach, *Phys. Plasmas* **23**, 101205 (2016).
- ¹⁴D. A. Yager-Elorriaga, Y. Y. Lau, P. Zhang, P. C. Campbell, A. M. Steiner, N. M. Jordan, R. D. McBride, and R. M. Gilgenbach, *Phys. Plasmas* **25**, 056307 (2018).
- ¹⁵C. E. Seyler, M. R. Martin, and N. D. Hamlin, *Phys. Plasmas* **25**, 062711 (2018).
- ¹⁶J. M. Woolstrum, D. A. Yager-Elorriaga, P. C. Campbell, N. M. Jordan, C. E. Seyler, and R. D. McBride, *Phys. Plasmas* **27**, 092705 (2020).
- ¹⁷P. C. Campbell, T. M. Jones, J. M. Woolstrum, N. M. Jordan, P. F. Schmit, J. B. Greenly, W. M. Potter, E. S. Lavine, B. R. Kusse, D. A. Hammer, and R. D. McBride, *Phys. Rev. Lett.* **125**, 035001 (2020).
- ¹⁸R. Reinovsky, W. Anderson, W. Atchison, C. Ekdahl, R. Faehl, I. Lindemuth, D. Morgan, M. Murillo, J. Stokes, and J. Shlachter, *IEEE Trans. Plasma Sci.* **30**, 1764 (2002).
- ¹⁹A. R. Miles, *Phys. Plasmas* **16**, 032702 (2009).
- ²⁰D. B. Sinars, S. A. Slutz, M. C. Herrmann, R. D. McBride, M. E. Cuneo, K. J. Peterson, R. A. Vesey, C. Nakhleh, B. E. Blue, K. Killebrew, D. Schroen, K. Tomlinson, A. D. Edens, M. R. Lopez, I. C. Smith, J. Shores, V. Bigman, G. R. Bennett, B. W. Atherton, M. Savage, W. A. Stygar, G. T. Leifeste, and J. L. Porter, *Phys. Rev. Lett.* **105**, 185001 (2010).
- ²¹Y. Y. Lau, J. C. Zier, I. M. Rittersdorf, M. R. Weis, and R. M. Gilgenbach, *Phys. Rev. E* **83**, 066405 (2011).
- ²²D. B. Sinars, S. A. Slutz, M. C. Herrmann, R. D. McBride, M. E. Cuneo, C. A. Jennings, J. P. Chittenden, A. L. Velikovich, K. J. Peterson, R. A. Vesey, C. Nakhleh, E. M. Waisman, B. E. Blue, K. Killebrew, D. Schroen, K. Tomlinson, A. D. Edens, M. R. Lopez, I. C. Smith, J. Shores, V. Bigman, G. R. Bennett, B. W. Atherton, M. Savage, W. A. Stygar, G. T. Leifeste, and J. L. Porter, *Phys. Plasmas* **18**, 056301 (2011).
- ²³R. D. McBride, S. A. Slutz, C. A. Jennings, D. B. Sinars, M. E. Cuneo, M. C. Herrmann, R. W. Lemke, M. R. Martin, R. A. Vesey, K. J. Peterson, A. B. Sefkow, C. Nakhleh, B. E. Blue, K. Killebrew, D. Schroen, K. Tomlinson, A. Laspe, M. R. Lopez, I. C. Smith, B. W. Atherton, M. Savage, W. A. Stygar, and J. L. Porter, *Phys. Rev. Lett.* **109**, 135004 (2012).
- ²⁴M. E. Cuneo, M. C. Herrmann, D. B. Sinars, S. A. Slutz, W. A. Stygar, R. A. Vesey, A. B. Sefkow, G. A. Rochau, G. A. Chandler, J. E. Bailey, J. L. Porter, R. D. McBride, D. C. Rovang, M. G. Mazarakis, E. P. Yu, D. C. Lamppa, K. J. Peterson, C. Nakhleh, S. B. Hansen, A. J. Lopez, M. E. Savage, C. A. Jennings, M. R. Martin, R. W. Lemke, B. W. Atherton, I. C. Smith, P. K. Rambo, M. Jones, M. R. Lopez, P. J. Christenson, M. A. Sweeney, B. Jones, L. A. McPherson, E. Harding, M. R. Gomez, P. F. Knapp, T. J. Awe, R. J. Leeper, C. L. Ruiz, G. W. Cooper, K. D. Hahn, J. McKenney, A. C. Owen, G. R. McKee, G. T. Leifeste, D. J. Ampleford, E. M. Waisman, A. Harvey-Thompson, R. J. Kaye, M. H. Hess, S. E. Rosenthal, and M. K. Matzen, *IEEE Trans. Plasma Sci.* **40**, 3222 (2012).
- ²⁵R. D. McBride, M. R. Martin, R. W. Lemke, J. B. Greenly, C. A. Jennings, D. C. Rovang, D. B. Sinars, M. E. Cuneo, M. C. Herrmann, S. A. Slutz, C. W. Nakhleh, D. D. Ryutov, J.-P. Davis, D. G. Flicker, B. E. Blue, K. Tomlinson, D. Schroen, R. M. Stamm, G. E. Smith, J. K. Moore, T. J. Rogers, G. K. Robertson, R. J. Kamm, I. C. Smith, M. Savage, W. A. Stygar, G. A. Rochau, M. Jones, M. R. Lopez, J. L. Porter, and M. K. Matzen, *Phys. Plasmas* **20**, 056309 (2013).
- ²⁶P. C. Campbell, T. M. Jones, J. M. Woolstrum, N. M. Jordan, P. F. Schmit, A. L. Velikovich, J. B. Greenly, W. M. Potter, E. S. Lavine, B. R. Kusse, D. A. Hammer, and R. D. McBride, *Phys. Plasmas* **28**, 082707 (2021).
- ²⁷P. Zhang, Y. Y. Lau, I. M. Rittersdorf, M. R. Weis, R. M. Gilgenbach, D. Chalenski, and S. A. Slutz, *Phys. Plasmas* **19**, 022703 (2012).
- ²⁸A. M. Steiner, P. C. Campbell, D. A. Yager-Elorriaga, K. R. Cochrane, T. R. Mattsson, N. M. Jordan, R. D. McBride, Y. Y. Lau, and R. M. Gilgenbach, *Phys. Plasmas* **25**, 032701 (2018).

- ²⁹D. D. Ryutov, T. J. Awe, S. B. Hansen, R. D. McBride, K. J. Peterson, D. B. Sinars, and S. A. Slutz, *AIP Conf. Proc.* **1639**, 63–66 (2014).
- ³⁰K. J. Peterson, D. B. Sinars, E. P. Yu, M. C. Herrmann, M. E. Cuneo, S. A. Slutz, I. C. Smith, B. W. Atherton, M. D. Knudson, and C. Nakhleh, *Phys. Plasmas* **19**, 092701 (2012).
- ³¹T. J. Smith, P. C. Campbell, G. V. Dowhan, N. M. Jordan, M. D. Johnston, M. E. Cuneo, G. R. Laity, and R. D. McBride, *Rev. Sci. Instrum.* **92**, 053550 (2021).
- ³²R. B. Baksht, A. S. Zhigalin, A. G. Rousskikh, and V. I. Oreshkin, *Phys. Plasmas* **27**, 043510 (2020).
- ³³R. B. Baksht, S. I. Tkachenko, A. S. Zhigalin, A. G. Rousskikh, and V. I. Oreshkin, *Phys. Plasmas* **28**, 062706 (2021).
- ³⁴C. E. Seyler, *Phys. Fluids B* **3**, 2449 (1991).
- ³⁵C. E. Seyler, *J. Geophys. Res.* **99**, 19513, <https://doi.org/10.1029/94JA01572> (1994).
- ³⁶C. E. Seyler and M. R. Martin, *Phys. Plasmas* **18**, 012703 (2011).
- ³⁷X. Zhang and C.-W. Shu, *J. Comput. Phys.* **229**, 8918 (2010).
- ³⁸A. Dedner, F. Kemm, D. Kröner, C.-D. Munz, T. Schnitzer, and M. Wesenberg, *J. Comput. Phys.* **175**, 645 (2002).
- ³⁹G. Tóth, *J. Comput. Phys.* **161**, 605 (2000).
- ⁴⁰M. R. Weis, Ph.D. thesis (University of Michigan, 2015).
- ⁴¹M. Desjarlais, *Contrib. Plasma Phys.* **41**, 267 (2001).
- ⁴²H. R. Strauss, *Phys. Fluids* **19**, 134 (1976).
- ⁴³Z. Kolberg, E. Liverts, and M. Mond, *Phys. Plasmas* **12**, 062113 (2005).
- ⁴⁴E. Liverts and M. Mond, *Phys. Plasmas* **11**, 55 (2004).
- ⁴⁵C. E. Seyler, *Phys. Plasmas* **27**, 092102 (2020).
- ⁴⁶P. Batten, N. Clarke, C. Lambert, and D. M. Causon, *SIAM J. Sci. Comput.* **18**, 1553 (1997).
- ⁴⁷P. C. Liewer and N. A. Krall, *Phys. Fluids* **16**, 1953 (1973).
- ⁴⁸R. C. Davidson and N. T. Gladd, *Phys. Fluids* **18**, 1327 (1975).
- ⁴⁹J. P. Chittenden, *Phys. Plasmas* **2**, 1242 (1995).